

# Determining Material Response for Polyvinyl Butyral (PVB) in Blast Loading Situations

P. Del Linz<sup>1,2</sup> · Y. Wang<sup>1</sup> · P.A. Hooper<sup>1</sup> · H. Arora<sup>1</sup> · D. Smith<sup>3</sup> · L. Pascoe<sup>3</sup> · D. Cormie<sup>3</sup> · B.R.K. Blackman<sup>1</sup> · J.P. Dear<sup>1</sup>

Received: 2 January 2016 / Accepted: 24 May 2016 / Published online: 17 June 2016  
© The Author(s) 2016. This article is published with open access at Springerlink.com

**Abstract** Protecting structures from the effect of blast loads requires the careful design of all building components. In this context, the mechanical properties of Polyvinyl Butyral (PVB) are of interest to designers as the membrane behaviour will affect the performance of laminated glass glazing when loaded by explosion pressure waves. This polymer behaves in a complex manner and is difficult to model over the wide range of strain rates relevant to blast analysis. In this study, data from experimental tests conducted at strain rates from  $0.01 \text{ s}^{-1}$  to  $400 \text{ s}^{-1}$  were used to develop material models accounting for the rate dependency of the material. Firstly, two models were derived assuming Prony series formulations. A reduced polynomial spring and a spring derived from the model proposed by Hoo Fatt and Ouyang were used. Two fits were produced for each of these models, one for low rate cases, up to  $8 \text{ s}^{-1}$ , and one for high rate cases, from  $20 \text{ s}^{-1}$ . Afterwards, a single model representing all rates was produced using a finite deformation viscoelastic model. This assumed two hyperelastic springs in parallel, one of which was in series with a non-linear damper. The results were compared with the experimental results, assessing the quality of the fits in the strain range of interest for blast loading situations. This should provide designers with the information to choose between the available models depending on their design needs.

**Keywords** Polyvinyl Butyral · Laminated glass · Strain rate sensitivity · Viscoelasticity

## Introduction

Explosions can put at risk the integrity of buildings during their service life. Glazing elements present a specific risk during such events, as their nature makes them more prone to catastrophic failures than other structural components, causing a large proportion of the injuries and economic losses occurring due to such loading [1].

Glass has relatively low fracture toughness and therefore will fail catastrophically without any plastic deformation. If simple annealed glass panes are used in a building, after their failure fragments can be thrown inside and outside the building envelope causing significant injuries. Additionally, once the building skin is pierced, the blast pressure waves are able to enter the internal spaces, causing additional wounds and damage. Composite laminated glass windows can be used to minimize the damage and risk of injury during blast events. Whilst the glass layers are expected to fracture under the applied pressures, the polyvinyl butyral (PVB) membrane will retain the glass fragments in the window frame. This ensures that no projectiles are created and that blast pressures do not enter the building space. Additionally, the glass fracture and the large subsequent displacements of the membrane provide a major mechanism to absorb the blast energy and mitigate its transfer to the supporting building structure, significantly reducing damage to these components. Figure 1 shows an example of such a laminated glass pane, showing its deformation mechanism after the glass fracture. Similar considerations also affect the design of forward facing aircraft windows, which have to resist significant pressures and potential high impact loads.

✉ J. P. Dear  
j.dear@imperial.ac.uk

<sup>1</sup> Department of Mechanical Engineering, Imperial College London, Exhibition Road, London SW7 2AZ, UK  
<sup>2</sup> Present address: School of Civil and Environmental Engineering, Nanyang Technological University, 50 Nanyang Avenue, Singapore 639798, Singapore  
<sup>3</sup> Arup Resilience Security and Risk, 13 Fitzroy Street, London W1T 4BQ, UK

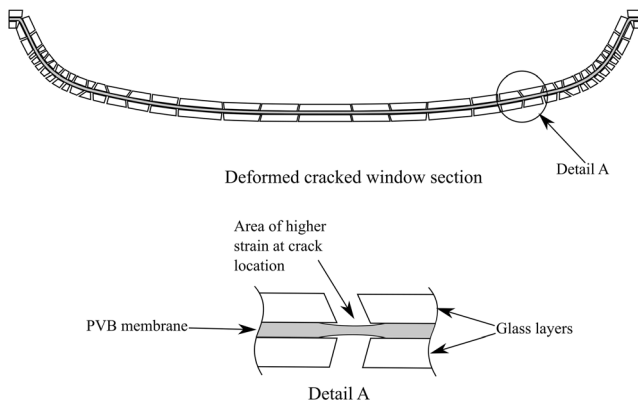


**Fig. 1** Deformation of laminated glass pane during a blast

Full scale blast tests have been performed in the past employing 3D digital image correlation (DIC) to provide full field strain and displacement data in three dimensions for the whole glass surface [2]. The glass panes were composed of two 3 mm thick plies of annealed glass with a 1.52 mm PVB interlayer. 12.8 and 25.6 kg C4 charges (15 and 30 kg TNT equivalent) were used and the stand-offs were between 10 and 16 m. These experimental data allowed the observation of the entire loading process, starting from blast wave arrival and including glass fracture and post-crack deformations. Typical graphical results are shown together with a diagram of the experimental set-up in Fig. 2, where the appreciable deformation of the PVB is apparent.

However, to provide improved design predictions for different blast situations, it is important to understand in detail the behaviour of all the laminated glass components, including the Polyvinyl Butyral (PVB) membrane. Specifically, relatively simple material models representing this material at the strain rates of interest would greatly assist the modelling of the entire structure and its behaviour under blast loading. These rates observed during blast events ranged from below  $1 \text{ s}^{-1}$  to above  $100 \text{ s}^{-1}$ , therefore models used would have to represent the material in this range. Additionally, the DIC results showed that the strain in the material is generally limited to 0.15 strain [2], making an appropriate characterisation of the material up to this deformation especially important.

The mechanical properties of this polymeric material have been the object of several studies. Vallabhan performed shear tests on laminated glass samples and obtained estimated of the shear modulus at different shear strain levels [3]. Du Bois and Timmel employed experimental results to include a hyperelastic model of the PVB material in their work. Several different spring functions were considered, using a Mooney Rivlin representation for their final impact model [4, 5]. Xu and Li have used experimental data to fit viscoelastic laws which were used for windscreen impact simulations [6]. Subsequently, they performed tests at high strain rate using a split Hopkinson bar apparatus to obtain stress–strain curves. They then fitted a viscoelastic law to this, assuming a

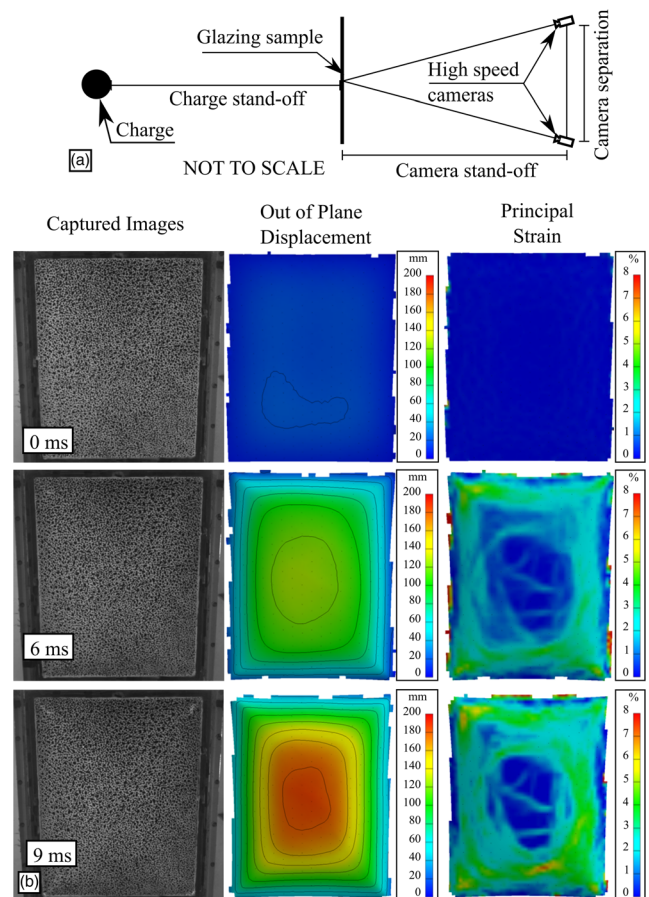


**Fig. 2** Typical blast and DIC set up and results from a blast test (30 kg TNT Equivalent at 16 m). The DIC set up is shown (not to scale) (a), together with a sample of the raw high speed images and DIC results at three time steps (b) (adapted from [2])

Mooney Rivlin hyperelastic spring to account for the non-linearity [7]. Iwasaki and Sato identified a shift in the PVB behaviour at high strain rates [8] and they included a material model fit for the lower strain rates cases [9]. Liu and Sun performed several tests at different strain rates both in tension and in compression. They then fitted the data with multiple individual material laws to cover the different rates and stress regimes [10]. Recently, Zhang et al. [11] also performed high rate tests on the PVB material, reaching rates beyond  $1000 \text{ s}^{-1}$ . The results of these authors also showed the same change in behaviour seen in previous studies.

In this research the properties of PVB polymer membranes were investigated to provide relevant material properties for use in future blast research and design projects. The aim of this study was to extend the available models to the high rates of deformation commonly seen in blast loading cases, whilst also attempting to limit the number of different models which would need to be used to account for the possible range of deformation speeds. Experimental data from uniaxial tests at different strain rates were employed to derive material models which could be used to model this component of the glazing

system. Three material models were fitted. These included two Prony series viscoelasticity functions and a model derived using a full mathematical solution of the finite deformation viscoelasticity equations. This last model assumed two different hyperelastic springs in parallel, one of which was placed in series with a viscous damper. The results from the various approaches were then compared considering their accuracy and their ease of application.

In all cases special attention was paid to the quality of the stress–strain fits up to 0.2 strains, which includes the range of strains generally seen in blast experimental data before the glazing samples reached ultimate failure.

## Method

### Experimental Programme

Tensile tests at different strain rates were performed on the same PVB material to obtain the data necessary for the model calibration. The material tested in all cases was Saflex PVB produced by Solutia Inc. with product number RB-41. The equipment used was different for the high and the low strain rate experiments, as no single machine could produce the range of desired speeds.

All the tests at rates above  $0.2 \text{ s}^{-1}$  and a proportion of the tests at rates below this were performed by Hooper et al. [12]. The samples were cut in a dog bone shape, with a height of 75 mm and a gauge length of 20 mm. The gauge length width was 4 mm and the material thickness was 0.76 mm throughout. The tests were performed on a servo-hydraulic Instron tensile testing machine, employing a loss motion device to ensure a more constant strain rate at the higher speeds. Lightweight titanium alloy grips were used to minimise inertial effects. Strain data were collected optically using a high speed camera and extracted with an automated image analysis algorithm. This consisted in locating two black lines drawn on the samples at 20 mm distance, measuring their relative position in each frame captured with high speed cameras. Photoelasticity techniques were also used for some samples to visualise the strain distribution. Though these results were not calibrated and hence could not be used to measure local strains directly, their results indicated a uniform strain distribution in the gauge length. Figure 3 is an image of one of the faster tests taken  $133 \mu\text{s}$  after the initial loading, indicating that the stresses exhibited a uniform distribution soon after the start of the test. Force data were collected using a piezoelectric load cell for speeds above  $0.1 \text{ m s}^{-1}$  and a strain gauge load cell for lower speeds. Tests were run at constant displacement speeds of 0.005, 0.1, 0.32, 1, 2, 5 and  $10 \text{ m s}^{-1}$ , providing results for average rates from 0.2 to  $400 \text{ s}^{-1}$ .

The lower rate tests, below and including  $0.2 \text{ s}^{-1}$  were performed for this study. The specimens in this case were

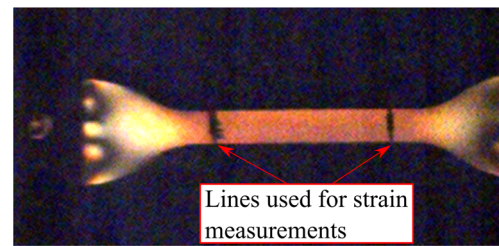


**Fig. 3** Photoelasticity results for a  $400 \text{ s}^{-1}$  test  $133 \mu\text{s}$  after the initial loading

cut following the dimensions specified in British Standard 37-2005 [13]. The plan geometry of the specimens is shown in Fig. 4, whilst their thickness was 1.52 mm.

A low load and low speed single column 1 kN Zwick tensile testing machine was employed. The strain data were collected optically in a manner similar to that used by Hooper et al. [12], with the difference that high speed cameras were not used in this case. A Matlab routine was employed to identify in the images black lines which had been drawn at regular intervals on the samples. The distance between these points could then be used to calculate the strain at each time step. The inbuilt force sensor of the machine was used to capture loading data. As relevant codes [14] are not prescriptive towards possible optical methods used for these measurements, both the method used here and previously by Hooper et al. [12] could satisfy the requirements. Tests were run at strain rates of 0.01, 0.02, 0.1 and  $0.2 \text{ s}^{-1}$ . All the tests were performed at a room temperature of  $20 \text{ }^\circ\text{C}$ . As the rooms were climate controlled, this temperature did not vary significantly during the tests. Whilst it is possible that the membrane temperature would have been increased during the test by the radiation produced by the explosion, it was assumed that this effect would have been of limited magnitude. It was nevertheless possible that the material temperature would have increased significantly due to the high rate deformation. However, the same effect would have taken place in the laboratory material tests, and would therefore be implicitly included in the results, justifying the use of these results to derive the desired material models.

The total number of tests at each speed is shown in Table 1. Both Hooper et al.'s [12] and new tests are listed, as both sets were employed in this analysis. In some cases the number of performed tests was less than three. The consistency of the

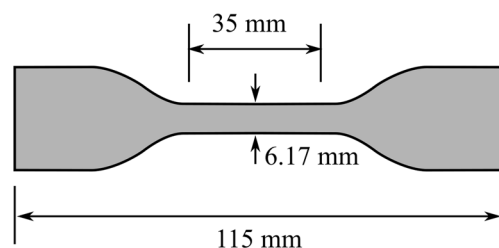


**Fig. 4** Dimension of specimens used in the low rate tests. The specimen thickness was 1.52 mm

**Table 1** Number of tests performed at each strain rate. Both Hooper's and new tests are listed

Rate (s <sup>-1</sup> )	0.01	0.02	0.1	0.2	2	8	20	60	200	400
Number of samples	3	3	3	5	2	2	5	3	5	8

tests was therefore considered when deciding to include the tests results.

Data from the two sets of experiments have been employed to produce material models for the PVB. As both sets of experiments produced data for the rate of 0.2 s<sup>-1</sup>, these curves have been compared. The other rates could not be compared, as they were covered only by one set of experiments.

### Material Model Fit

The experimental results highlighted the high degree of rate dependence of the PVB material. Material models need to take this into account and ideally include a mechanism to represent this change in behaviour. Hooper et al. [12] argued that a viscoelastic model employing a Prony series would not be able to cover all the strain rates of interest. This was because, for the model to be able to represent all the rates, its stretch and time dependant components needed to be independent and separable. As this was not possible in the PVB data, it could be assumed a single model would not be able to represent the range of behaviours observed regardless of the number of terms used. Specifically, it was challenging to ensure that a single Prony series model would show the changes in the small strain stiffness observed in the experiments. This issue could be overcome by using different models for different rate conditions. As an example, the models proposed by Liu et al. [9] represented different strain rate ranges and loading types and hence ensured all the material behaviours of interest were covered.

However, work by several authors, for example that of Hoo Fatt and Ouyang [15] shows that models which exhibit the desired change in behaviour can be derived using finite deformation viscoelasticity laws. Through these, different hyperelastic models can be combined, ensuring that the whole range of deformation speeds is covered. The technique has been described thoroughly by Huber and Tsakmakis [16] and has been used by Hoo Fatt and Ouyang [15], Arruda and Boyce [17], Amin et al. [18, 19] and others.

In this work both approaches were attempted. Firstly, two Prony series models were developed using different hyperelastic models, specifically a Hoo Fatt model and a reduced polynomial model. As it was not possible to model the entire PVB behaviour with a single set of parameters [12], two parameter fits were performed for each hyperelastic

formulation, one for the lower strain rate and one for the higher strain rate data sets. In this case, the “low rate” model covered tests up to and including an average rate of 8 s<sup>-1</sup>, whilst the “high rate” models covered rates higher than 8 s<sup>-1</sup>. The rigorous finite deformation viscoelasticity derivation was then employed to formulate a single model covering the entire range of rates. This required the use of different hyperelastic springs and a nonlinear viscosity function. The different material models are described in more detail below.

### Basic assumptions and definitions

When deriving the material models described above, certain assumptions were made with regards to the PVB behaviour. The coordinates of a point in the material before deformations take place ( $t = 0$ ) are defined by the vector  $\mathbf{X}$ . If this element of material is moved by the deformation, its new coordinates will be given by a new vector,  $\mathbf{x}$ . The deformation tensor  $\mathbf{F}$  is given by  $F_{ij} = \frac{\partial x_i}{\partial X_j}$ . The material was considered incompressible for this study. This implies that the product of the diagonal members of the deformation tensor should be 1. Therefore, if  $F_{11}$  is equal to the stretch ratio ( $\lambda$ ),  $F_{22}$  and  $F_{33}$  will be equal to  $\frac{1}{\sqrt{\lambda}}$ . For uniaxial tension,  $\mathbf{F}$  will therefore be equal to:

$$\mathbf{F} = \begin{bmatrix} \lambda & 0 & 0 \\ 0 & \frac{1}{\sqrt{\lambda}} & 0 \\ 0 & 0 & \frac{1}{\sqrt{\lambda}} \end{bmatrix} \quad (1)$$

The left Cauchy-Green strain tensor  $\mathbf{B}$  is given by  $\mathbf{B} = \mathbf{F}\mathbf{F}^T$ . Therefore, in this case:

$$\mathbf{B} = \begin{bmatrix} \lambda^2 & 0 & 0 \\ 0 & \frac{1}{\lambda} & 0 \\ 0 & 0 & \frac{1}{\lambda} \end{bmatrix} \quad (2)$$

The two invariants of  $\mathbf{B}$  are defined by  $I_1 = \text{tr}(\mathbf{B}) = \lambda^2 + 2\lambda^{-1}$  and  $I_2 = \frac{1}{2} \left\{ (\text{tr}(\mathbf{B}))^2 - \text{tr}(\mathbf{B}\mathbf{B}) \right\} = \lambda^{-2} + 2\lambda$ .

These quantities, especially  $\mathbf{B}$  and its invariants, were used to derive all the material models.

### Prony series derivation

These viscoelastic material models include a non-linear hyperelastic function  $\sigma_0(\varepsilon)$ , dependent on strain, combined with a Prony series,  $g(t)$ , to include the time dependency. The overall material model for a step strain relaxation test is shown in equation. (3):

$$\sigma = \sigma_0(\varepsilon) \times g(t) \quad (3)$$



The hyperelastic function was derived from the basic Equation [17]:

$$\mathbf{T} = -p\mathbf{I} + 2 \frac{\partial\psi}{\partial I_1} \mathbf{B} - 2 \frac{\partial\psi}{\partial I_2} \mathbf{B}^{-1} \tag{4}$$

where  $\mathbf{T}$  is the Cauchy true stress tensor. The function implies that a function representing the work of the spring ( $\psi$ ) needs to be differentiated with respect to the first two strain invariants of the strain tensor  $\mathbf{B}$ . Lamber-Diani and Rey [20] argued that to determine the portion of the equation relating to  $I_2$ , a biaxial test would be required. As this was not available here, work functions related solely to  $I_1$  were chosen for this analysis. This would limit the applicability of the model, as it would be validated only for single axis test, and applying it to heavily biaxial situations would represent an extrapolation from the available data. However, in the proposed application, as shown in Fig. 1, the PVB membrane will stretch significantly in the direction perpendicular to the crack lines, therefore representing a uniaxial tension situation.

The time dependent function  $g(t)$  was assumed to take the form of a Prony series, which for stress relaxation test data is given by:

$$g(t) = g_\infty + \sum_1^N g_i \exp\left(-\frac{t}{\tau_i}\right) \tag{5}$$

where  $g_\infty$ , the long term shear modulus,  $g_i$  and  $\tau_i$  are model parameters to be found. The model parameter fit was performed assuming six terms of this series, using either the  $\tau_i$  terms derived by Hooper or others at more regular logarithmic intervals to facilitate the fitting process. The method described by Goh et al. [21] was employed to perform the material model fit, applying a square minimisation technique to determine the coefficients. The Solver function of Microsoft Excel 2012 was used to solve the optimisation problem.

*Hoo fatt formulation*

Hoo Fatt and Ouyang [15] used a model similar to an Ogden spring when deriving a material law for a polymer material. The rationale for this formulation was to be able to represent the sharp change in stiffness which took place at small strains. As the behaviour of the material under consideration here is similar, the same hyperelastic law has been employed. However, in this case the model was expanded into a summation in a similar manner to the classic Ogden model. This allowed the sharp stiffness change to be reproduced with a single hyperelastic spring in the Prony series approach. The work function used is:

$$\psi = \sum_i \mu_i (I_1 - 3)^{\alpha_i} \tag{6}$$

where  $\mu_i$  and  $\alpha_i$  are model parameters to be found. Two terms were used. If this function is substituted into equation (4), the hyperelastic strain is given by:

$$\mathbf{T} = -p\mathbf{I} + 2\alpha_1\mu_1(I_1-3)^{(\alpha_1-1)}\mathbf{B} + 2\alpha_2\mu_2(I_1-3)^{(\alpha_2-1)}\mathbf{B} \tag{7}$$

The term  $p$  in the equation above can be found considering the boundary conditions  $\sigma_{22} = \sigma_{33} = 0$ . Substituting into equation (7), a formula for  $p$  is derived:

$$p = 2\alpha_1\mu_1(I_1-3)^{(\alpha_1-1)}\frac{1}{\lambda} + 2\alpha_2\mu_2(I_1-3)^{(\alpha_2-1)}\frac{1}{\lambda} \tag{8}$$

and therefore the final hyperelastic expression for uniaxial tension is given by:

$$\sigma_{11} = 2\left(\lambda^2 - \frac{1}{\lambda}\right)\left(\alpha_1\mu_1(I_1-3)^{(\alpha_1-1)} + \alpha_2\mu_2(I_1-3)^{(\alpha_2-1)}\right) \tag{9}$$

*Reduced polynomial formulation*

Various authors in the past have used a polynomial formulation to represent the PVB material, for example Muralidhar et al. [22]. As discussed above, a model independent of  $I_2$  had to be used in this case. Therefore a reduced polynomial formulation [23] was chosen in this work. Whilst this model does not guarantee an equally accurate representation of the change in stiffness at higher rates, it was considered that this procedure would ensure the straightforward application of the model in finite element software for further analysis of the composite material.

The work function in this case is given by:

$$\psi = \sum_i C_i (I_1 - 3)^i \tag{10}$$

where  $C_i$  are constants to be found. A third order model was employed. Using the function above with equation (4) the stress tensor was:

$$\mathbf{T} = -p\mathbf{I} + 2\left(C_1 + 2C_2(\mathbf{I}_1 - 3) + 3C_3(\mathbf{I}_1 - 3)^2\right)\mathbf{B} \tag{11}$$

The term  $p$  could be found using the same method described above, giving:

$$p = 2\left(C_1 + 2C_2(\mathbf{I}_1 - 3) + 3C_3(\mathbf{I}_1 - 3)^2\right)\frac{1}{\lambda} \tag{12}$$

Inserting this in equation (11) and deriving an equation for  $\sigma_{11}$  gave:

$$\sigma_{11} = 2\left(\lambda^2 - \frac{1}{\lambda}\right)\left(C_1 + 2C_2(\mathbf{I}_1 - 3) + 3C_3(\mathbf{I}_1 - 3)^2\right) \tag{13}$$



### Finite Deformation Viscoelasticity

#### Model derivation

The finite deformation viscoelasticity models are derived by solving the mathematical equations representing a “springs and dampers” system, similar to those assumed in traditional viscoelasticity theory. However, in this case all small strain assumptions are avoided to produce a solution valid for any level of deformation. For the situation of interest here a system of two nonlinear springs and a damper was assumed, as shown in Fig. 5. This is the same system as Model A described by Huber and Tsakmakys [16], and was also used by several other authors previously mentioned [15, 19].

The total observed stress is equal to the sum of the stresses affecting each spring. The single spring is referred to as the equilibrium spring (“eq” in symbols), whilst the spring in series with the damper is referred to as the overstress spring (“oe” in symbols). The deformation of the equilibrium spring and the summation of that of the damper and overstress spring series is the same and equal to the overall measured deformation. Therefore, as shown in Fig. 5, the deformation of the equilibrium spring is equal to  $\mathbf{B}$ . The deformation of the overstress spring is instead dependant on the viscous behaviour of the damper, introducing a time dependency in the model.

Huber and Tsakmakys [16] and Hoo Fatt and Ouyang [15] provided a detailed derivation of the general equations governing this model. The first step of the method, introduced by Lubliner [24] in the context of finite deformation plasticity, is to decompose the overall system deformation into an equilibrium and an instantaneous part,  $\mathbf{F} = \mathbf{F}_e \mathbf{F}_i$ .  $\mathbf{F}_i$  represents the deformation state which would be reached if the load was instantaneously removed from the deformed sample. It could therefore be associated with the deformation of the damper.  $\mathbf{F}_e$

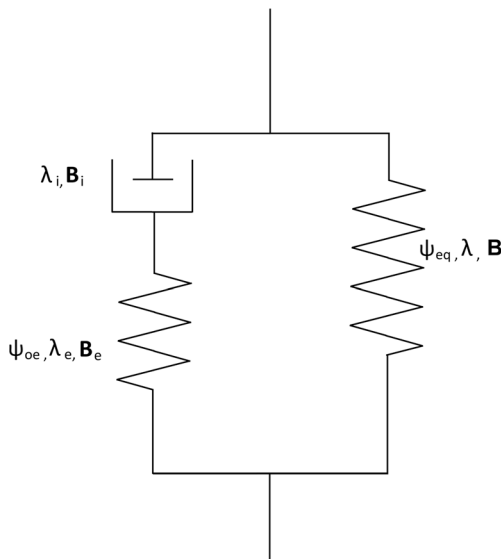


Fig. 5 A summary of the material model assumed to model PVB

is instead assumed to be the deformation of the overstress spring, hence the strain responsible for the stress acting in the damper and spring series.

Additionally, it is assumed that the system will obey the thermodynamic condition [19]:

$$-\rho_r \dot{\psi} + \mathbf{S}_E \cdot \mathbf{L} \geq 0 \tag{14}$$

Where  $\rho_r$  is the material mass density in the original configuration,  $\dot{\psi}$  is the rate of change of the internal Helmholtz free energy,  $\mathbf{S}_E$  is Cauchy (true) stress and  $\mathbf{L}$  is the velocity gradient,  $\mathbf{L} = \dot{\mathbf{F}} \mathbf{F}^{-1}$ , measuring the rate of change of the velocity in the volume of the material at a given moment in time.

Huber and Tsakmakys showed the derivation of a system of equations based on these assumptions, and concluded with a material model given by:

$$\mathbf{T} = -p\mathbf{I} + 2 \frac{\partial \psi_{eq}}{\partial I_{1B}} \mathbf{B} - 2 \frac{\partial \psi_{eq}}{\partial I_{2B}} \mathbf{B}^{-1} + 2 \frac{\partial \psi_{oe}}{\partial I_{1B_e}} \mathbf{B}_e - 2 \frac{\partial \psi_{oe}}{\partial I_{2B_e}} \mathbf{B}_e^{-1} \tag{15}$$

$$\mathbf{B}_e = \mathbf{L} \mathbf{B}_e + \mathbf{B}_e \mathbf{L}^T - \frac{2}{\eta} \mathbf{B}_e \mathbf{T}_{oe} \tag{16}$$

Where  $\mathbf{T}_{oe} = 2 \frac{\partial \psi_{oe}}{\partial I_{1B_e}} \mathbf{B}_e - 2 \frac{\partial \psi_{oe}}{\partial I_{2B_e}} \mathbf{B}_e^{-1}$ ,  $\mathbf{B}_e$  is the left Cauchy-Green strain tensor for the overstress spring and  $\eta$  represents the viscosity function of the damper. Spring functions similar to those derived above for the Prony series models can then be substituted into the equations. This derivation method was used here, assuming a one term Ogden [25] function for the equilibrium spring and a three terms Hoo Fatt’s spring function for the overstress response. Substituting these springs into the system above, the following equations were obtained for uniaxial tension:

$$\sigma_{11} = \mu_o \lambda^{\alpha_o} - \mu_o \lambda^{-\frac{1}{2}\alpha_o} + 2 \left( \lambda_e^2 - \frac{1}{\lambda_e} \right) \times \left( \alpha_1 \mu_1 (I_{1B_e} - 3)^{(\alpha_1 - 1)} + \alpha_2 \mu_2 (I_{1B_e} - 3)^{(\alpha_2 - 1)} + \alpha_3 \mu_3 (I_{1B_e} - 3)^{(\alpha_3 - 1)} \right) \tag{17}$$

$$\mathbf{B}_e = \mathbf{L} \mathbf{B}_e + \mathbf{B}_e \mathbf{L}^T - \frac{2}{\eta} \mathbf{B}_e 2 \left( \lambda_e^2 - \frac{1}{\lambda_e} \right) \times \left( \alpha_1 \mu_1 (I_{1B_e} - 3)^{(\alpha_1 - 1)} + \alpha_2 \mu_2 (I_{1B_e} - 3)^{(\alpha_2 - 1)} + \alpha_3 \mu_3 (I_{1B_e} - 3)^{(\alpha_3 - 1)} \right) \tag{18}$$

The parameters of these equations were fitted using the method explained below.

**Data fit method** Hoo Fatt and Ouyang presented a method to fit the model constants for this kind of mathematical representation. In their paper, the constants for the two springs were obtained first. At low, quasi static, rates it was assumed that the damper would offer no resistance to the deformation.

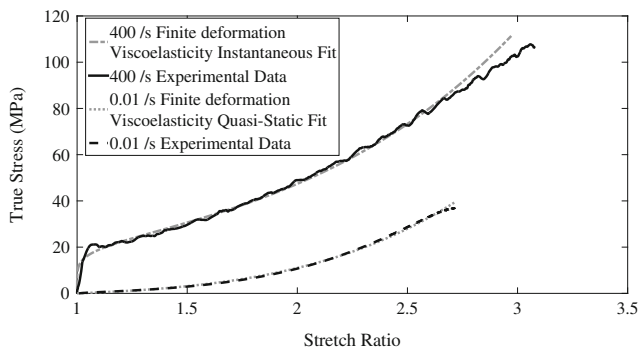


**Fig. 6** The lowest and highest available strain rate data were used to fit the two spring models for the finite deformation viscoelasticity model. The figure shows the raw data and the model fits

Therefore, the overstress spring would not be stretched, giving  $F_i = F$  and  $F_e = I$ . The measured stress would therefore be caused by the deformation of the equilibrium spring. Therefore, data sets in this range of rates could be used to fit the parameters of the equilibrium spring directly. As the two lowest strain rates data available were similar (see Fig. 11), it was assumed that the quasi static condition was being approached. The Ogden model spring could then be fitted with the data from the lowest rate experiment ( $0.01 \text{ s}^{-1}$ ).

Again, the data for the higher rates, at 200 and  $400 \text{ s}^{-1}$ , showed less variation than data at lower speeds. It was therefore assumed that these sets would approximate an instantaneous response of the material. In this condition, it could be assumed that the damper would not move, and hence that the overstress spring deformation would be equal to the total deformation of the material, specifically  $F_i = I$  and  $F_e = F$ . As the total measured stress was equal to the sum of the stresses acting on the two springs and the equilibrium spring stress could be calculated using the material constants obtained in the previous (quasi static) step, the stress acting on the overstress spring could be found. This allowed a stress strain curve to be derived for the overstress spring, whose material parameters could then be fitted. This procedure was followed using the  $400 \text{ s}^{-1}$  data.

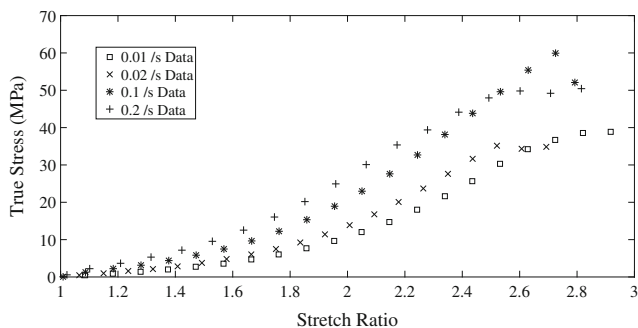


**Fig. 7** Low rate true Stress - stretch curves for PVB under uniaxial tensile loading. Only the recent data for the  $0.2 \text{ s}^{-1}$  case are presented for clarity

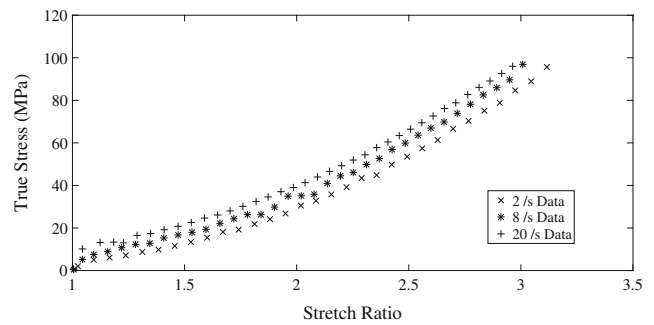


**Fig. 8** Intermediate rate true stress – stretch curves for PVB under uniaxial tensile loading

Figure 6 shows the two extreme stress-stretch curves together with the fitted models. Once the parameters of the springs had been fitted, the viscous function had to be considered. The data showed that a constant would not be sufficient to model the different material behaviour. A function as used by Hoo Fatt and Ouyang was assumed and the parameters were fitted to the data. To achieve this, the method described in the same paper was followed. This assumed a matrix  $F_e$  of the form:

$$F_e = \begin{pmatrix} \lambda_e & 0 & 0 \\ 0 & \frac{1}{\sqrt{\lambda_e}} & 0 \\ 0 & 0 & \frac{1}{\sqrt{\lambda_e}} \end{pmatrix} \quad (19)$$

Therefore  $B_e$  was equal to:

$$B_e = \begin{pmatrix} \lambda_e^2 & 0 & 0 \\ 0 & \frac{1}{\lambda_e} & 0 \\ 0 & 0 & \frac{1}{\lambda_e} \end{pmatrix} \quad (20)$$

Using this assumption,  $\lambda$  and  $\lambda_e$  could be substituted in the overstress strain rate differential equation, which became:

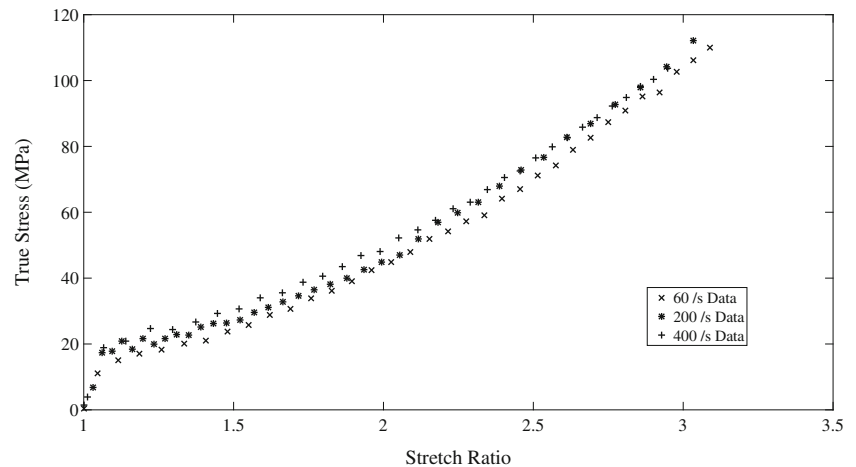
$$\lambda_e = \frac{\lambda \lambda_e}{\lambda} - \frac{2T_{oe}}{3\eta} \lambda_e \quad (21)$$

Therefore  $\eta = \frac{2\lambda \lambda_e T_{oe}}{3(\lambda \lambda_e - \lambda_e \lambda)}$ . The values of  $\eta$  found in this way were fitted to the proposed equation:

$$\eta = \{C_{\eta 1}(1 - \exp(C_{\eta 2}(I_{1B_e} - 3))) + C_{\eta 3}\} (C_{\eta 4} I_{1B_e}^3 + C_{\eta 5} I_{1B_e}^2 + C_{\eta 6} I_{1B_e} + C_{\eta 7}) \quad (22)$$

This function was substituted into the system of equations of the model. Values for  $\eta$  and the required deformation invariants were obtained from the available data.  $T_{oe}$  was calculated by subtracting the equilibrium spring stress from the experimentally measured stress. This data was used to calculate  $\lambda_e$  from the known overstress spring

**Fig. 9** High rate true stress – stretch curves for PVB under uniaxial tensile loading



equation. As the equation for this was nonlinear and difficult to invert, the stretch was found using a numerical solver in Matlab [26]. The overstress rate was then found through numerical differentiation. A polynomial was fitted to the  $\lambda_e$  data to achieve this, since otherwise the noise present in the experimental curve would have prevented realistic estimates being obtained. The values of  $\eta$  obtained were then used to fit the constants required.

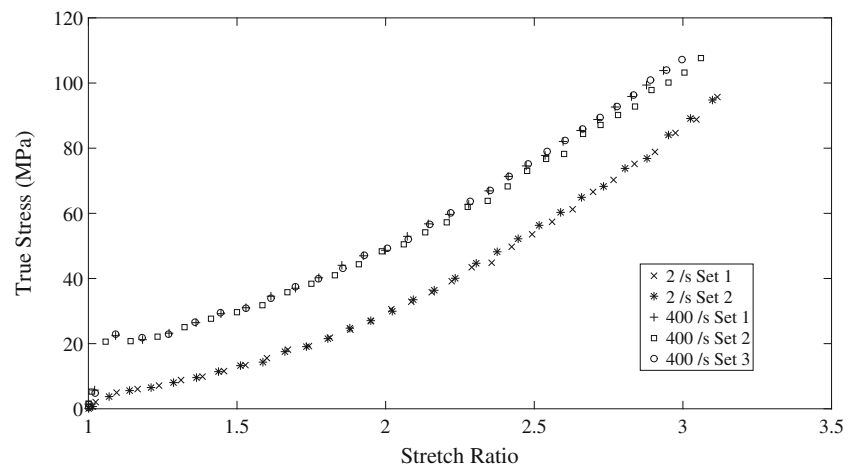
Once the parameters were obtained, the resulting system of equations was solved numerically using Matlab.

## Results

### Experimental Results

The results from both sets of experiments are presented together for clarity.

**Fig. 10** Two typical data sets for each of the rates  $2 \text{ s}^{-1}$  and  $400 \text{ s}^{-1}$  are shown. The curves are very similar, showing that the experimental results were consistent between the various repetitions



The data is shown as true stress versus stretch ratio  $\lambda$ , which is equal to the length of the sample at time  $t$  ( $l_t$ ) over the original length ( $l_0$ ):

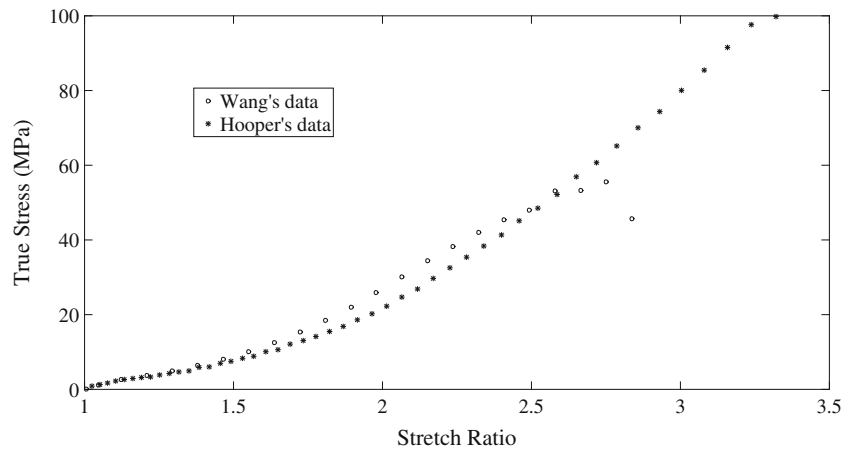
$$\lambda(t) = \frac{l_t}{l_0} \quad (23)$$

The results of the low rate tests are shown in Fig. 7. As expected the curves presented nonlinear behaviour together with significant strain rate sensitivity. At these rates the shape of the curves did not change significantly, mostly showing an increase in the overall stiffness as the deformation speed increased.

The tests performed at strain rates above and including  $2 \text{ s}^{-1}$  are shown in Figs. 8 and 9. The material non linearity was still very evident, as was the rate sensitivity. Additionally the shapes of the curves at the higher strain rates, starting from a rate of  $8 \text{ s}^{-1}$ , changed significantly, exhibiting a much higher stiffness at small strains. This was consistent with past



**Fig. 11** Comparison of results from Hooper [12] and Wang at the strain rate  $0.2 \text{ s}^{-1}$



observations by Iwasaki and Sato [9]. The effect became marked for rates of  $20 \text{ s}^{-1}$  and above. Ideally a PVB material model used for finite element application should be able to represent this switch in behaviour to ensure that all situations could be modelled accurately.

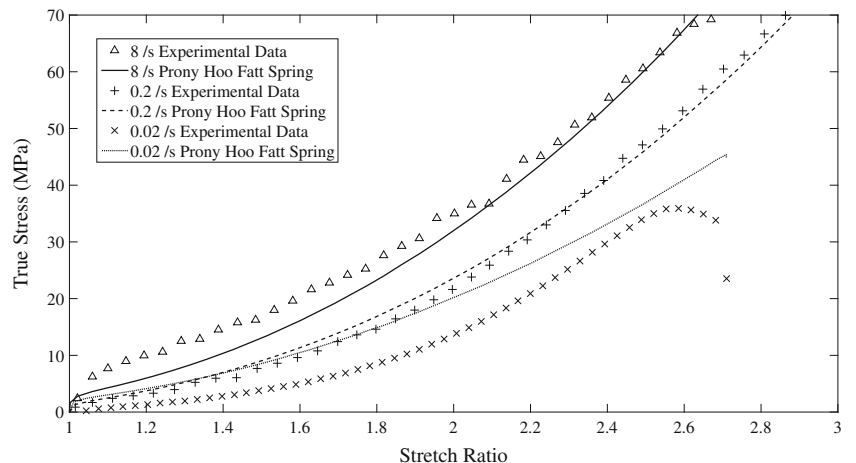
The failure point of the material did not change significantly with the rate, the final stretch varying between  $\approx 2.7$  and  $\approx 3.2$  depending on the specific test. In one of the tests at a rate of  $200 \text{ s}^{-1}$  the grips appeared to have slipped at a stretch of roughly 2.5, prejudicing the accuracy of the results beyond this point. However, other data sets show the full behaviour up to a failure stretch of 3, as shown in Fig. 9.

All data sets were employed for further analysis, though generally only one data set is shown for each speed for clarity. Typical curves for  $2 \text{ s}^{-1}$  and  $400 \text{ s}^{-1}$  are shown in Figure 10, showing several experimental data sets for each of the strain rates. The results are typical for the other tested rates. The data were consistent between each experimental repeat, with small differences if compared with the likely accuracy of model fits. Therefore, all rates were employed in the analysis, even though in some cases less than three tests were performed for a specific strain rate.

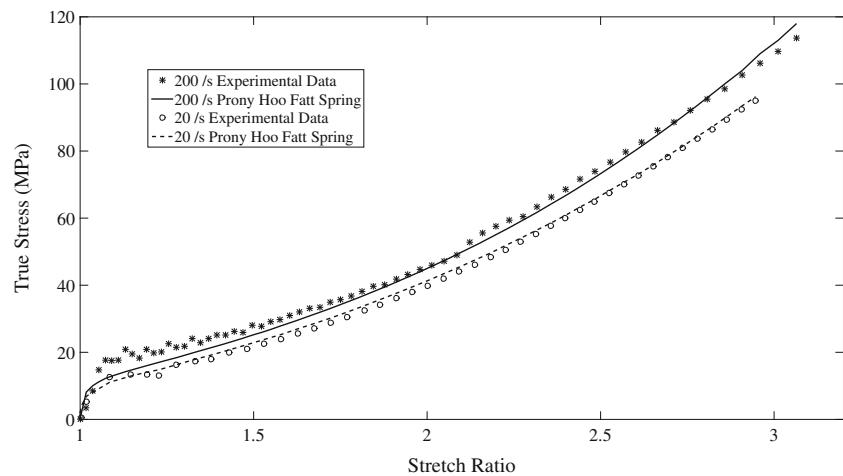
The faster rates were also likely to present some more uncertainty with regards to the exact initial modulus of the material. Whilst photoelasticity results showed that the strains were uniformly distributed after the very initial sample loading stage, Hooper et al. [12] calculated that for the  $400 \text{ s}^{-1}$  case, the rise time predicted with an assumed initial stiffness would be similar to the time taken by a stress wave to travel the length of the sample,  $40 \mu\text{s}$ , prejudicing the exact stiffness measurement in the early times. Zhang et al. [11] however measured longer initial yield times with a similar set up and material. This suggested the initial results were valid, as suggested here by the photoelasticity results shown in Fig. 3. Whilst this should guarantee an acceptable homogenization of the stresses, it is possible that other effects, such as the instrumentation free vibrations, will affect the precision of the initial stiffness estimates. However, due to the expected precision of the models used, it is unlikely that the uncertainty associated with these issues will prejudice the evaluation of the proposed material models.

Figure 11 shows a plot of the results at  $0.2 \text{ s}^{-1}$  from both tests performed by Hooper et al. and the latest series of experiments. The curves were similar, with maximum differences of

**Fig. 12** Low strain rate Prony series with Hoo Fatt spring fit for tests at rates  $0.02, 0.2$  and  $8 \text{ s}^{-1}$ . Hooper's data are shown for the  $0.2 \text{ s}^{-1}$  case



**Fig. 13** High strain rate Prony series with Hoo Fatt spring fit for tests at rates 20 and 200  $s^{-1}$



4 MPa. Below a stretch of 1.5 this was limited to 2 MPa, with the curves superimposing in the most relevant range up to 1.2 stretch. The failure points were often lower in the second series of experiments, where the samples failed at a stretch of 2.7 instead of the 3.2 limit reached in Hooper et al.'s data. This was due to the difference in the sample geometry. Thicker and wider samples were used in the later experiments, causing higher forces to be applied to achieve the same stretch levels. Therefore, eventual imperfections in the sample shape lead to higher levels of stress concentrations, causing earlier specimen failures. However, in both cases the failures took place at significantly higher strain levels than the range of interest. Therefore, it was decided that both the stress and failure limit deviations would not affect the accuracy of the material models significantly and the data from the two sets of experiments were used directly without applying corrections.

### Prony Series - Hoo Fatt Spring

Figure 12 shows the experimental data and the fitted material models for a selection of low strain rate (up to 8  $s^{-1}$ ) cases. The plots show that this function did not represent the material behaviour accurately at the lowest strain rate of 0.02  $s^{-1}$ . The fit improved for the intermediate rate of 0.2  $s^{-1}$ . However, the quality decreased again for the higher rate of 8  $s^{-1}$ , where the initial behaviour was not captured by the

**Table 2** Material parameters for the Hoo Fatt's spring

Parameter	Low rate (up to 8 $s^{-1}$ )	High rate (above to 20 $s^{-1}$ )
$\eta_1$ (MPa)	4.37	8.1
$\alpha_1$	1.38	1.54
$\eta_2$ (MPa)	5.68	95.7
$\alpha_2$	0.618	0.68

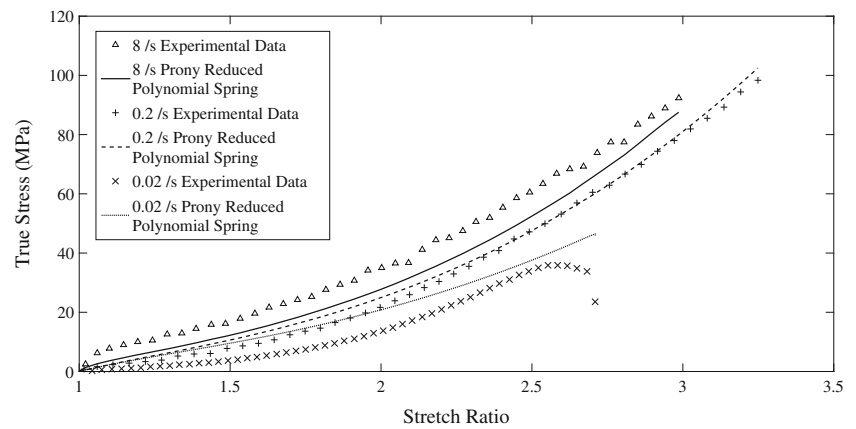
model. Whilst the shapes of the stress-stretch curves showed some change throughout the range of rates, it is at 8  $s^{-1}$  that the stress curve started to show the increase in initial stiffness that cannot be modelled by the basic hyperelastic spring.

Figure 13 show the data for the high strain rate (from 20  $s^{-1}$ ) cases. The model showed some initial stiffness and followed the experimental results at higher stretches more accurately than the low rate cases. However, the fit again seemed to be of lower quality for the highest rate cases, where the initial stiffness did not match the experimental stiffness. The model though followed again the experimental data accurately after this stage. Figures 19, 20 and 21 show plots of the errors for selected strain rates up to 1.2 stretch, the useful range for blast loading simulation, and will be discussed below. Tables 2 and 3 summarise the parameters which were used in both the low and high rate cases.

**Table 3** Prony series parameters for the Hoo Fatt's spring viscoelastic model

Parameter	Low rate (up to 8 $s^{-1}$ )	High rate (above to 20 $s^{-1}$ )
$\tau_1$ (s)	$1 \times 10^{-4}$	$1 \times 10^{-6}$
$g_1$	0	0.569
$\tau_2$ (s)	$1 \times 10^{-3}$	$1 \times 10^{-5}$
$g_2$	0.200	0.161
$\tau_3$ (s)	$1 \times 10^{-2}$	$1 \times 10^{-3}$
$g_3$	0	.00996
$\tau_4$ (s)	0.1	0.1
$g_4$	0.274	.0269
$\tau_5$ (s)	1	10
$g_5$	0	0
$\tau_6$ (s)	100	1000
$g_6$	0.526	0
$g_{inf}$	0	0.143

**Fig. 14** Low strain rate Prony series with the reduced polynomial spring fit for tests at rates 0.02, 0.2 and 8 s<sup>-1</sup>. Hooper's data are shown for the 0.2 s<sup>-1</sup> case

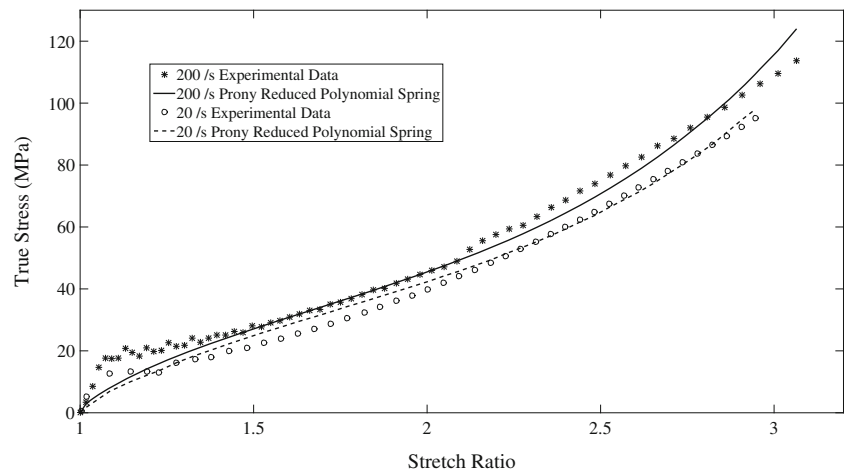


### Prony Series – Reduced Polynomial Spring

The fitting of the reduced polynomial spring model was again performed for the low strain rate and the high strain rate cases separately. The low strain rate (up to 8 s<sup>-1</sup>) results are shown in Fig. 14. The results were similar to those for the Hoo Fatt spring model. The model followed the experimental data for the 0.2 s<sup>-1</sup> data set. However, the lower and the higher rates were less accurate. The lower rates stiffness was overestimated, producing higher stresses than those produced experimentally. Instead, the 8 s<sup>-1</sup> case again showed that the model could not capture the initial stiffness, producing lower stresses than recorded in the experiment.

The results of the fit for the higher strain rates (above 20 s<sup>-1</sup>) are shown in and Fig. 15. In this case the model results were accurate once the material softened, without though modelling the initial deformation. This was probably due to limitations in the spring model used. Tables 4 and 5 show the parameters which were used for these fits, whilst Figs. 19, 20 and 21 show again the error in the fits at several strain rates.

**Fig. 15** High strain rate Prony series with the reduced polynomial spring fit for tests at rates 20 and 200 s<sup>-1</sup>



### Finite Deformation Viscoelasticity

Figures 16 and 17 show selected plots of the experimental data with their respective model fits obtained using finite deformation viscoelasticity. At the lower rates the model showed some noise at low stretches, up to about  $\lambda = 1.1$ . This was due to the difficulty of reaching a stable numerical solution for the non-linear differential equation in these cases. The accuracy of the fit was again lower for the 8 s<sup>-1</sup> rate. However, in this case the model overestimated the initial stiffness rather than underestimating it as in the Prony series results. Both the lowest rates, such as 0.02 s<sup>-1</sup> and the intermediate ones, such as 8 s<sup>-1</sup>, showed more accurate results than the Prony series models. For the rates of 0.1 and 0.2 s<sup>-1</sup> instead the model did not show enough stiffness, reducing its accuracy.

Figure 17 indicates that the model was able to represent the initial stiffness seen in the experiments. Therefore, the model was shown to be able to switch between the high rate behaviour and the low rate behaviour, as can be seen by the difference between the 200 and the 0.02 s<sup>-1</sup> curves.

**Table 4** Material parameters for the reduced polynomial hyperelastic spring

Parameter	Low rate (up to $8 \text{ s}^{-1}$ )	High rate (above to $20 \text{ s}^{-1}$ )
C1 (MPa)	40.7	311
C2 (MPa)	75.7	0.0112
C3 (MPa)	0	1.3

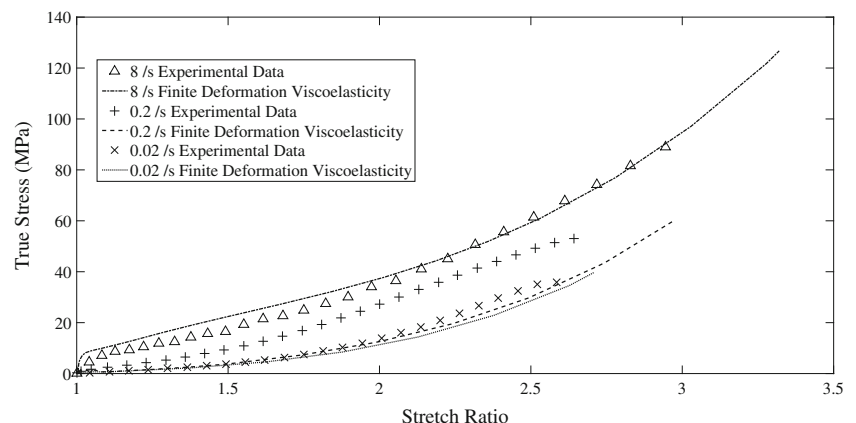
**Table 5** Prony series parameters for the reduced polynomial viscoelastic model

Parameter	Low rate (up to $8 \text{ s}^{-1}$ )	High rate (above to $20 \text{ s}^{-1}$ )
$\tau_1$ (s)	$1 \times 10^{-4}$	$1 \times 10^{-6}$
$g_1$	0	0
$\tau_2$ (s)	$1 \times 10^{-3}$	$1 \times 10^{-5}$
$g_2$	0.898	0.948
$\tau_3$ (s)	$1 \times 10^{-2}$	$1 \times 10^{-3}$
$g_3$	0	0.0151
$\tau_4$ (s)	0.1	0.1
$g_4$	0	0.00112
$\tau_5$ (s)	1	10
$g_5$	0	0
$\tau_6$ (s)	100	1000
$g_6$	0.102	0
$g_{\text{inf}}$	0	0.0354

Tables 6 and 7 show the parameters which were fitted for the two springs.

## Discussion

All the models could capture aspects of the PVB behaviour at the various strain rates, though showing different limitations.

**Fig. 16** Finite deformation viscoelasticity material model fit for rates 0.02, 0.2 and  $8 \text{ s}^{-1}$ 

As highlighted previously by Hooper et al. [12], the experimental results available showed a change in the material behaviour taking place between the rates of 2 and  $20 \text{ s}^{-1}$ , with the initial stiffness rising rapidly in this range. After this, the initial stiffness appeared to remain constant, hence it could be assumed that further increases in rate would not increase this parameter significantly. However, the peak stress before the material relaxation increased somewhat between the two higher rate sets of tests (200 and  $400 \text{ s}^{-1}$ ). Therefore, it is possible that this parameter might increase further should the material be deformed at higher rates. This further increase was also confirmed in the newer data produced by Zhang et al. [11].

The changes in the data also highlighted the need for separate material models, as discussed in the method section. As an example, the high rate curves produced by the low rate Hoo Fatt spring Prony series is shown in Fig. 18. The plots show that the fit results display too low stiffness, as the increased initial stiffness is not represented in the model.

The Prony series models for low rates struggled to represent the data at both the bottom and the top end of their rate range. They produced stresses greater than measured for the slower tests, whilst the  $8 \text{ s}^{-1}$  curve fits did not show the initial stiffness and hence underestimated stresses. The high rate (above  $20 \text{ s}^{-1}$ ) fits showed a good agreement beyond the initial high stiffness region. Both models though struggled to account accurately for the low strain deformations, especially for the 200 and  $400 \text{ s}^{-1}$  cases. This error was much smaller in the Hoo Fatt spring model, which showed the needed behaviour, albeit without reaching the correct stress levels. The reduced polynomial model instead struggled to show the initial stiffness in any of the high rate cases and employing more terms to improve this caused the results to show significant oscillation, precluding their use in finite element models. After the initial stiffness phase though the high rate models produced a better fit than the low rate models. The greater accuracy of the high strain rate fits might be due to the fact that the

**Fig. 17** Finite deformation viscoelasticity model fit for rates 20 and 200 s<sup>-1</sup>

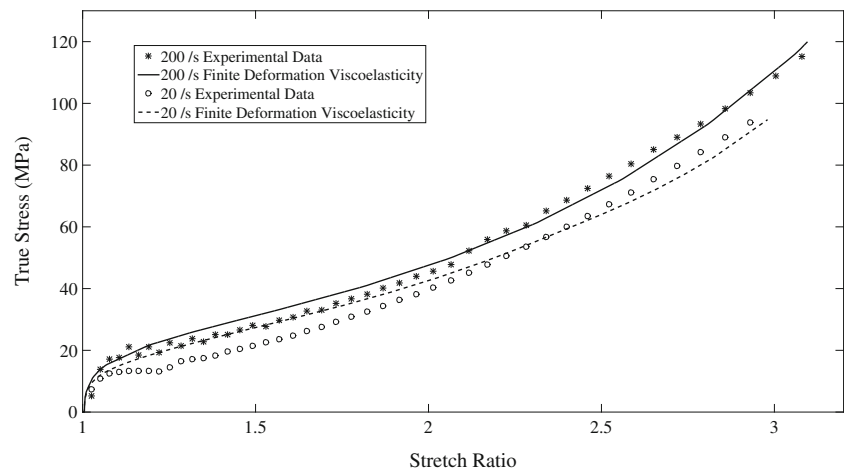


**Table 6** Hyperelastic spring parameters for finite deformation viscoelasticity

$\mu_0$ (MPa)	$\alpha_0$	$\mu_1$ (MPa)	$\alpha_1$	$\mu_2$ (MPa)	$\alpha_2$	$\mu_3$ (MPa)	$\alpha_3$
0.632	4.141	117.373	0.746	16.035	0.806	-121.468	0.768

shape of the stress stretch curves for these cases shows relatively less variation, allowing a single model to capture their behaviour. These results indicate that at least a third model could be fitted covering the intermediate rates, including 8 s<sup>-1</sup>. More experiments would be needed at rates of similar magnitude to achieve this.

The rigorous finite deformation viscoelasticity was able to fit accurately more of the data sets considered. Again, the fit quality was lower at lower stretches, though generally better than the Prony Series models as shown in Figs. 19 and 21, however it tended to improve significantly as the deformation increased. Additionally, the model could represent the higher stiffness region at high strain rate employing just one set of constants, thereby opening the possibility of using a single model to represent the PVB material for a range of situations. This however, came at the cost of greater model complexity, both in terms of the model derivation and of the procedure needed to fit the material constants.

Figures 19, 20 and 21 show plots of the absolute errors for strain rates of 0.02, 0.2 and 200 s<sup>-1</sup> up to a stretch of 1.2. These data were calculated by subtracting the modelled

stresses from the experimental stresses at each point. The absolute error was chosen as at the relevant stretches the stresses were generally small, which implied that small absolute errors would produce very large relative errors. This would be especially the case for the lower strain rate cases, as the absolute value of the stresses was significantly smaller, often below 10 MPa, increasing the apparent importance of errors in these cases. A similar set of information is shown in Table 8, which gives the mean square error between stretches of 1 and 1.15 for each fit. The absolute error for the finite deformation model, was lower for both the 0.02 s<sup>-1</sup> and the 200 s<sup>-1</sup>, i.e., the curves are closer to 0. Whilst this behaviour was common to several other rates considered, it should be noted that, as shown in Fig. 20, the Prony series models are more accurate at the rates of 0.1 and 0.2 s<sup>-1</sup>. These results were also largely confirmed by the mean square error, which summarised the quality of the fits in a single value. Whilst this did not highlight the difference in accuracy at different levels of deformation, it represented a useful comparison between the models. Again, it could be seen that, in general, the finite deformation elasticity model produced similar or improved fits at most strain rates, especially at the lower and higher ends of the tested range. The fit quality instead was similar and in occasions slightly worse between 0.1 and 8 s<sup>-1</sup>, in the transition between the low and high rate behaviour. However, the error magnitude at the stretches of interest was still relatively low, up to 2 MPa. The most likely cause of this inaccuracy was the nature of the differential equation which needs to be solved as

**Table 7** Damping function parameters for finite deformation viscoelasticity

$C\eta_1$ (MPa s)	$C\eta_2$	$C\eta_3$ (MPa s)	$C\eta_4$	$C\eta_5$	$C\eta_6$	$C\eta_7$
1.131	-0.248	0.026	-1.527	6.626	4.876	-5.893



**Fig. 18** The high rate cases (above  $20 \text{ s}^{-1}$ ) curves produced with the low rate Prony series with Hoo Fatt spring model. The model shows significantly lower stiffness than seen in the experiments

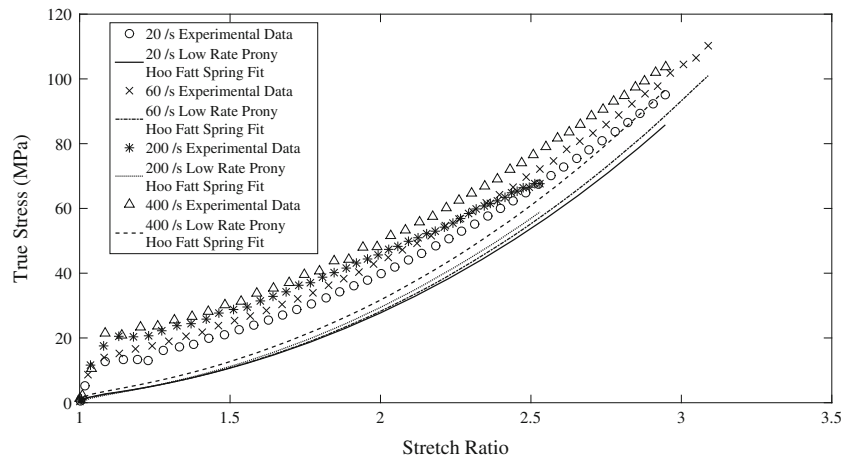
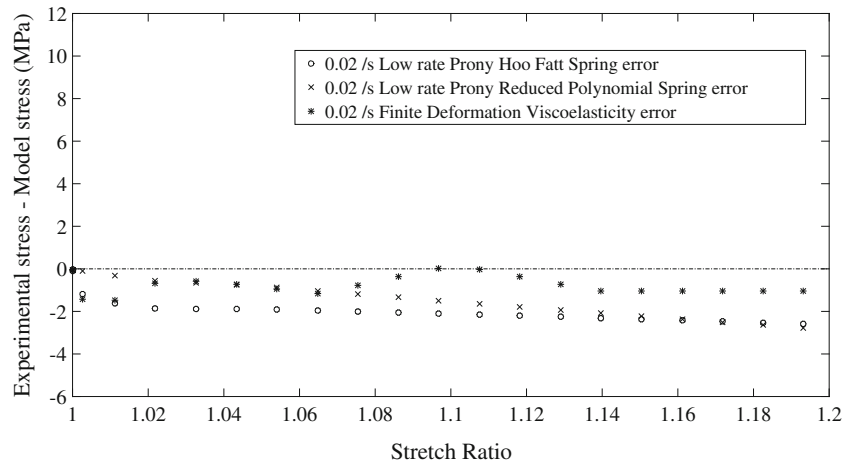


**Fig. 19** Fit absolute errors for the  $0.02 \text{ s}^{-1}$  strain rate case calculated subtracting the models stresses by the experimental values. The low rate Prony series models were used. The Finite Deformation Viscoelasticity model produced a more accurate fit in most of the considered range



part of the material model. The shape of the stress–strain relations for the materials indicated a sharp change of initial stiffness between the rates of 2 and  $20 \text{ s}^{-1}$ . Whilst the equations used here were able to represent the change, their behaviour was not perfect, as the differential equations required to model this sudden change were very stiff. Therefore, the

relatively small changes in the material stiffness in the lower rate models were not represented fully by the material model. The errors introduced by this issue were of approximately 2.5 MPa in the stretch range of interest, as shown in Fig. 20. In the situation considered though, the PVB membrane was likely to deform at such low rates especially when still

**Fig. 20** Fit absolute errors for the  $0.2 \text{ s}^{-1}$  strain rate case calculated subtracting the models stresses by the experimental values. The low rate Prony series models were used and produced a more accurate fit in most of the considered range, with errors of less than 2 MPa

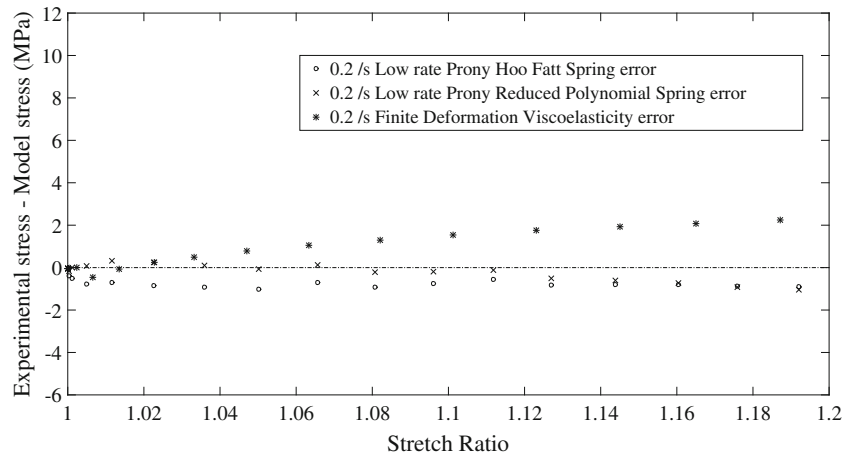
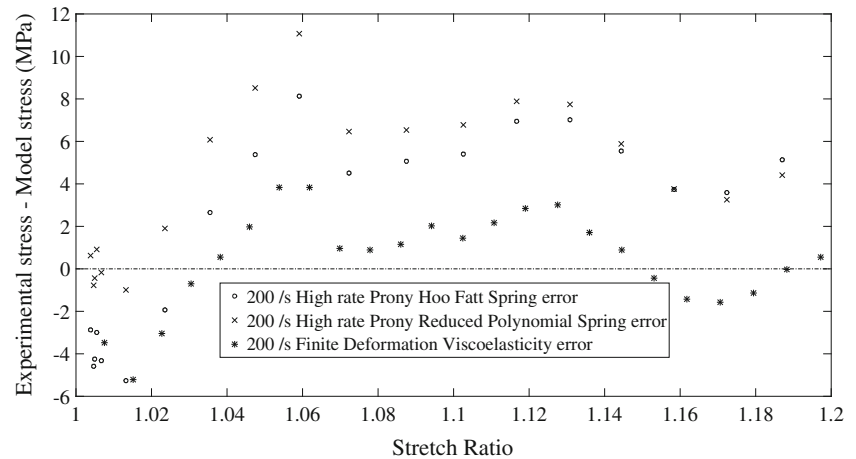


**Fig. 21** Fit absolute errors for the  $200 \text{ s}^{-1}$  strain rate case calculated subtracting the models stresses by the experimental values. The high rate Prony series models were used. The Finite Deformation Viscoelasticity model produced a more accurate fit in most of the considered range, with errors between  $-6$  and  $4 \text{ MPa}$ , instead of up to  $12 \text{ MPa}$  in the Prony series case



connected with the glass layers. In this situations, as discussed previously, its strains and stresses would be small, as the significantly stiffer glass layers would limit the membrane deformations. Whilst this phase of the deformation would need to be modelled, as the composite action of the glazing material depends on the stresses transferred by the PVB, it was assumed that the uncertainties would be less important than those affecting the material behaviour after its separation from the glass. The deformation at this stage though would take place at much higher strain rates, generally within the more accurately represented high rate regime. Therefore, the ability of representing a low strain behaviour, though somewhat less precise, together with the change in stiffness at higher rate and an accurate representation of the high rate stress–strain relationships would be useful for modelling the blast loading phenomenon.

Therefore, in general the figures show that the fit produced with the finite strain viscoelasticity model tended to be of similar or better quality than those of the Prony series models in the stretch range of interest. Additionally, as mentioned, the results were produced using a single model and set of

constants, rather than switching between two separate models for different strain rate regimes as per the Prony series. Therefore, whilst in specific cases a specific Prony series model might produce more precise results, the more complex finite strain viscoelasticity model guarantees much more flexibility for possible design models.

## Conclusion

The PVB tensile experimental data demonstrated the high level of non-linearity and strain rate dependency exhibited by this material. Two methods have been used to produce several material models which account for this shift in behaviour. In the first approach, two hyperelastic functions were used to produce four separate Prony series viscoelastic models. These were fitted to the high rate experimental data, including  $20 \text{ s}^{-1}$  and above, and to the low rate experimental data, including  $8 \text{ s}^{-1}$  and below.

These models produced more accurate results for the high rate fits, especially at larger stretch levels, even though the

**Table 8** Mean square error of the fits between 1 and 1.15 stretches

Rate ( $\text{s}^{-1}$ )	Prony Hoo Fatt Spring ( $\text{MPa}^2$ )	Prony Reduced Polynomial Spring ( $\text{MPa}^2$ )	Finite Deformation Viscoelasticity ( $\text{MPa}^2$ )
0.01	3.9	1.9	0.2
0.02	3.6	1.6	0.2
0.1	2.1	0.4	0.4
0.2	0.6	0.1	0.9
2	1.2	2.7	2.3
8	8.8	8.2	10.4
20	5.7	13.5	4.4
60	5.9	29.2	4.8
200	25.9	33.5	5.7
400	31.6	23.0	12.4

quality deteriorated somewhat at higher rates. The Hoo Fatt spring performed better at lower stretches, as it was better able to represent the rapid change in stiffness. The low rate fits instead did not manage to capture the change in behaviour of the material in the range considered. This caused them not to represent accurately the small strain behaviour of the fastest case,  $8 \text{ s}^{-1}$ , as the experimental curve began to show an initial higher stiffness at this rate. The behaviour of the lower rate data sets was also not captured accurately. These results suggest that, ideally, a third Prony series model might be needed for intermediate strain rates.

To overcome the Prony series limitations, a finite viscoelasticity model was also derived following the method reported by Huber and Tsakmakys [16]. This was shown to account for the range of rates considered, with generally more accurate results than the Prony series models, except for the rates of  $0.1 \text{ s}^{-1}$  and  $0.2 \text{ s}^{-1}$ . However, both the model derivation and fitting procedure were significantly more complex and the model required a large number of constants to be determined (eight for the springs and seven for the damper). Also, as the model is not currently included in commercially available finite element software, a user material subroutine would need to be developed in order to apply it.

If the blast deformation phase of interest can be limited to a specific small range of strain rates, it would be advantageous to employ one of the Prony series viscoelastic models, as these require fewer constants to be included and they are commonly supported by FE software. However, if the rates of interest are not known or are spread over a larger range, the finite viscoelasticity model might well prove advantageous. In this case the large number of constants to be fitted would still be smaller than the total number of parameters for both the Prony series models and the overall accuracy would be improved.

The combination of the models presented in this paper are appropriate in modelling the complex behaviours of laminated glass panes during blast loading and under extreme impact loading when strain rates of interest cover a wide range.

**Acknowledgments** The authors wish to acknowledge the Arup Resilience Security and Risk with the Engineering and Physical Sciences Research Council (EPSRC) for supporting Dr Paolo Del Linz during his PhD on blast performance of laminated glass and AVIC Beijing Institute of Aeronautical Materials (BIAM), through the AVIC Centre for Material Characterisation, Processing and Modelling, for supporting Yi Wang during his PhD on impact performance of laminated glass windows. The authors also thank Dr John A. Crosse, Dr Maria Charalambides and Professor Michelle S. Hoo Fatt for their very helpful discussions on the theories employed in this research.

**Open Access** This article is distributed under the terms of the Creative Commons Attribution 4.0 International License (<http://creativecommons.org/licenses/by/4.0/>), which permits unrestricted use, distribution, and reproduction in any medium, provided you give appropriate credit to the original author(s) and the source, provide a link to the Creative Commons license, and indicate if changes were made.

## References

- Sukhran R (2005) Selection of glazing materials for blast protection. Glass Processing Days, Finland
- Hooper PA, Sukhran RAM, Blackman BRK, Dear JP (2012) On the blast resistance of laminated glass. *Int J Solids Struct* 49(6):899–918. doi:10.1016/j.ijsolstr.2011.12.008
- Vallabhan C, Das Y, Ramasamudra M (1992) Properties of PVB interlayer used in laminated glass. *J Mater Civ Eng* 4(1):71–76. doi:10.1061/(ASCE)0899-1561(1992)4:1(71)
- Du Bois PA, Kolling S, Fassnacht W (2003) Modelling of safety glass for crash simulation. *Comput Mater Sci* 28(3–4):675–683. doi:10.1016/j.commatsci.2003.08.023
- Timmel M, Kolling S, Osterrieder P, Du Bois PA (2007) A finite element model for impact simulation with laminated glass. *Int J Impact Eng* 34(8):1465–1478. doi:10.1016/j.ijimpeng.2006.07.008
- Xu J, Li Y (2009) Crack analysis in PVB laminated windshield impacted by pedestrian head in traffic accident. *Int J Crashworthiness* 14(1):63–71. doi:10.1080/13588260802462427
- Xu J, Li Y, Ge D, Liu B, Zhu M (2011) Experimental investigation on constitutive behavior of PVB under impact loading. *Int J Impact Eng* 38(2–3):106–114. doi:10.1016/j.ijimpeng.2010.10.001
- Iwasaki R, Sato C (2006) The influence of strain rate on the interfacial fracture toughness between PVB and laminated glass. *J Phys IV France* 134:1153–1158
- Iwasaki R, Sato C, Latailladeand JL, Viot P (2007) Experimental study on the interface fracture toughness of PVB (polyvinyl butyral)/glass at high strain rates. *Int J Crashworthiness* 12(3):293–298. doi:10.1080/13588260701442249
- Liu B, Sun Y, Li Y, Wang Y, Ge D, Xu J (2012) Systematic experimental study on mechanical behavior of PVB (polyvinyl butyral) material under various loading conditions. *Polym Eng Sci* 52(5):1137–1147. doi:10.1002/pen.22175
- Zhang X, Hao H, Shi Y, Cui J (2015) The mechanical properties of Polyvinyl Butyral (PVB) at high strain rates. *Constr Build Mater* 93:404–415. doi:10.1016/j.conbuildmat.2015.04.057
- Hooper PA, Blackman BRK, Dear JP (2012) The mechanical behaviour of poly(vinyl butyral) at different strain magnitudes and strain rates. *J Mater Sci* 47(8):3564–3576. doi:10.1007/s10853-011-6202-4
- British Standard Institution (2005) BS ISO 37-2005: Rubber, vulcanized or thermoplastic - Determination of tensile stress-strain properties. London
- British Standard Institution (2002) BS ISO 5893-2002: Rubber and plastics test equipment - Tensile, flexural and compression types (constant rate of traverse) - Specification. London
- Hoo Fatt MS, Ouyang X (2008) Three-dimensional constitutive equations for Styrene Butadiene Rubber at high strain rates. *Mech Mater* 40(1–2):1–16. doi:10.1016/j.mechmat.2007.06.002
- Huber N, Tsakmakis C (2000) Finite deformation viscoelasticity laws. *Mech Mater* 32(1):1–18. doi:10.1016/S0167-6636(99)00045-9
- Arruda EM, Boyce MC (1993) A three-dimensional constitutive model for the large stretch behavior of rubber elastic materials. *J Mech Phys Solids* 41(2):389–412. doi:10.1016/0022-5096(93)90013-6
- Amin A, Alam MS, Okui Y (2002) An improved hyperelasticity relation in modeling viscoelasticity response of natural and high damping rubbers in compression: experiments, parameter identification and numerical verification. *Mech Mater* 34(2):75–95. doi:10.1016/S0167-6636(01)00102-8
- Amin A, Lion A, Sekita S, Okui Y (2006) Nonlinear dependence of viscosity in modeling the rate-dependent response of natural and high damping rubbers in compression and shear: Experimental



- identification and numerical verification. *Int J Plast* 22(9):1610–1657. doi:[10.1016/j.ijplas.2005.09.005](https://doi.org/10.1016/j.ijplas.2005.09.005)
20. Lambert-Diani J, Rey C (1999) New phenomenological behavior laws for rubbers and thermoplastic elastomers. *Eur J Mech A Solids* 18(6):1027–1043. doi:[10.1016/S0997-7538\(99\)00147-3](https://doi.org/10.1016/S0997-7538(99)00147-3)
  21. Goh SM, Charalambides MN, Williams JG (2004) Determination of the constitutive constants of Non-linear viscoelastic materials. *Mech Time Depend Mater* 8(3):255–268. doi:[10.1023/B:MTDM.0000046750.65395.fe](https://doi.org/10.1023/B:MTDM.0000046750.65395.fe)
  22. Muralidhar S, Jagota A, Bennison SJ, Saigal S (2000) Mechanical behaviour in tension of cracked glass bridged by an elastomeric ligament. *Acta Mater* 48(18–19):4577–4588. doi:[10.1016/S1359-6454\(00\)00244-5](https://doi.org/10.1016/S1359-6454(00)00244-5)
  23. Yeoh OH (1993) Some Forms of the Strain Energy Function for Rubber. *Rubber Chem Technol* 66(5):754–771. doi:[10.5254/1.3538343](https://doi.org/10.5254/1.3538343)
  24. Lubliner J (1980) *Plasticity theory*. Macmillan Publishing, New York
  25. Ogden RW (1972) Large deformation isotropic elasticity - on the correlation of theory and experiment for incompressible rubberlike solids. *Proc Royal Soc Lond A Math Phys Sci* 326(1567):565–584. doi:[10.1098/rspa.1972.0026](https://doi.org/10.1098/rspa.1972.0026)
  26. MathWorks (2012) MATLAB - Documentation. [www.mathworks/help/matlab](http://www.mathworks/help/matlab)